Reconfigurable Resonant Topology Linking Two-, Three-, and Four-Coil Modes for WPT With Large Coupling Range and Fixed Frequency

Wenxing Zhong, *Senior Member, IEEE*, Siyuan Zhang, Min Chen, *Senior Member, IEEE*, and Mark Dehong Xu, *Fellow, IEEE*

***Abstract*—In wireless power transfer (WPT) applications, it is usually desired to transfer full power from the transmitter to the receiver in a position range as large as possible. However, the full-power operation range of a WPT system is typically designed for a small position range. This article proposes a reconfigurable resonant topology adopting the splitting coil structure in both the primary and secondary sides. The proposed reconfigurable resonant topology can output high power when the air gap varies in a wide range. Simulation and experimental results are provided to demonstrate that the proposed reconfigurable resonant topology can output full power in a large coupling range without significantly increasing the VA rating of the system. The measured dc–dc efficiency of the 3.3-kW prototype in an air gap range of 95–215 mm is 92%–95%.**

***Index Terms*—IPT, reconfigurable resonant topology, WPT.**

I. Introduction

THE wireless power transfer (WPT) technology will be widely adopted for charging electric vehicles and all kinds of robots in the near future. A lot of efforts have been devoted to developing advanced wireless charging techniques [1]–[4], [35]. One of the main challenges of wireless charging is the wide coupling range caused by parking position deviations and different chassis heights of different types of vehicles.

Conventional WPT systems cannot transfer rated power over a wide coupling range without significantly increasing the volt-ampere (VA) capacity of the system. Among many compensation topologies, series-series (SS) is widely used due to its simplicity. However, one critical issue of SS WPT is that its output power decreases as the coupling increases if the operating frequency is fixed. Moreover, frequency splitting occurs in the overcoupling range [5]–[9]. Therefore, if an SS system with a fixed operating frequency needs to output a rated power in a wide coupling range, its VA capacity must be significantly increased [4] because the output power of such a system is determined by the product of the mutual inductance and the primary and secondary currents.

In order to improve the power transfer capability of SS systems in strongly coupled regions, several methods have been proposed, such as the following.

1) Under the condition of strong coupling, the operating frequency is changed to the splitting frequencies to effectively increase the output power [6], [10]. However, this method needs to adjust the operating frequency, which relies on complicated control circuits. Moreover, the frequency-tuning control is sensitive to the resonant frequencies of the coupled resonators. With different parameters, the gain–frequency characteristic of the system will be different and might affect the control and soft switching of the primary inverter.
2) Many studies have been carried out on higher order compensation topologies [11]–[14], especially on the inductance–capacitance–capacitance (*LCC*) compensation [15]–[19]. Studies have shown that *LCC* can better cope with the misalignment conditions compared with SS [19], which implies that higher order compensation topologies may help to improve the power transmission capability of the system with a wide coupling range. However, according to the results in [15] and [19], when the *LCC* systems work at the worst-coupling positions (i.e., with the largest air gap and the largest misalignment), the output powers of the systems drop significantly.
3) Methods have been proposed based on switchable capacitor [20]–[23], switchable winding structure [24]–[28], or reconfigurable *LC* resonator structure [29]. These methods can change the inherent impedance characteristics of the system to improve the performance of the system in a wide coupling range.

A four-coil coupled structure, consisting of one drive coil (or power coil), one transmitter coil (or Tx coil), one receiver coil (or Rx coil), and one load coil, was proposed in [30]. The Tx and Rx coils are self-resonant utilizing the parasitic capacitances of the coils or lumped capacitors as the resonant capacitances, and they are not connected to other circuits. Compared with the

Manuscript received August 11, 2021; revised January 2, 2022; accepted January 25, 2022. Date of publication February 1, 2022; date of current version March 24, 2022. This work was supported in part by the National Natural Science Foundation of China under Grant 51807174 and in part by the Fundamental Research Funds for the Central Universities of China under Grant 2021FZZX001-12. Recommended for publication by Associate Editor J.-I. Itoh. *(Corresponding authors: Min Chen; Mark Dehong Xu.)*

The authors are with the Institute of Power Electronics, Zhejiang University, Hangzhou 310027, China (e-mail: wxzhong@zju.edu.cn; 21960050@zju.edu.cn; heaven@zju.edu.cn; xdh@zju.edu.cn).

Color versions of one or more figures in this article are available at https://doi.org/10.1109/TPEL.2022.3148001.

Digital Object Identifier 10.1109/TPEL.2022.3148001

typical two-coil WPT system, the four-coil system offers more degrees of freedom for impedance matching, which is essential to achieve higher output power and/or higher power transfer efficiency. In [31], the transmitter coil of a two-coil WPT system is split into two, one for the drive coil connected to the source and one for the relay coil. Using this structure, the efficiency drop caused by the source impedance can be largely eliminated. By changing the parameters of the four coils, e.g., the number of turns of the relay coil [32] or the diameter of the driving coil [28], the power transfer capability and/or efficiency can be improved in a large coupling range. In [29], a reconfigurable resonant topology based on a splitting receiver coil is proposed. The system can operate in the conventional two-coil mode, or the three-coil mode with one receiver-side relay resonator, and thereby significantly improve the power transfer efficiency for a large coupling range.

A reconfigurable resonant topology with four operation modes, i.e., the 1-to-1, 1-to-2, 2-to-1, and 2-to-2 modes, is proposed in this article. Each operation mode has a different coupling and compensation structure and can transfer full power within a different coupling range. The full-power coverage ranges of the 1-to-1, 1-to-2, and 2-to-1 modes are theoretically derived under practical input voltage and current constraints. Based on this, the strategy of linking four operations modes to enable the system to output full power in a substantially larger coupling range is investigated in simulations. A 3.3-kW prototype is built, and experimental results confirm the operation of the proposed reconfigurable resonant topology.

The rest of this article is organized as follows. Section II reviews the issue of a conventional SS WPT system with a case study. Section III first introduces the concept of the reconfigurable resonant topology, then proposes one practical implementation of the conceptual topology, and theoretically analyzes four operation modes of the topology. Simulation and experimental verifications are given in Section IV. Finally, Section V concludes this article.

II. Issue of Conventional SS WPT

The structure of the couplers, the circuit topology, and the fundamental harmonic approximation (FHA) circuit model of a conventional SS WPT system are shown in Fig. 1 , Fig. 2, and Fig. 3, respectively. The FHA circuit equations of the system are given in (1) and (2) [5]

$$(R_P + jX_P)\mathbf{I_{in}} + j\omega M_{PS}\mathbf{I}_O = \mathbf{V_{in}} \tag{1}$$

$$j\omega M_{PS}\mathbf{I_{in}} + (R_S + R_L + jX_S)\mathbf{I}_O = \mathbf{0} \tag{2}$$

where $X_i = \omega L_i - 1/(\omega C_i)$, L_i, C_i, and R_i, $i = P$ or S, are the reactance, the self-inductance, the compensating capacitance, and the equivalent series resistance of resonator-i, respectively; M_{PS} is the mutual inductance; R_L is the equivalent load resistance; ω is the operating angular frequency; $\mathbf{V_{in}}$ and $\mathbf{I_{in}}$ are the input voltage and input current in phasor representation, respectively; $\mathbf{I_o}$ is the phasor of the output current.

An SS WPT system outputs less power when the coupling becomes stronger if the operating frequency is fixed at the resonant frequency. Therefore, the coupling range in which an SS WPT system with a fixed operating frequency can output the required full power is normally small. An example is given as follows. In the example system, the rated power is set at 3.3 kW; the input and output dc voltages are both 400 V, and the operating frequency is 85 kHz, which is adapted for a fixed-frequency WPT system by the Society of Automotive Engineers standard J2954 [34]. Table I lists the parameters of the system.

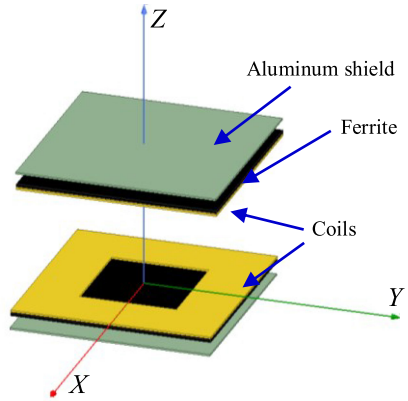

Fig. 1. Structure of the couplers of a conventional two-coil WPT system.

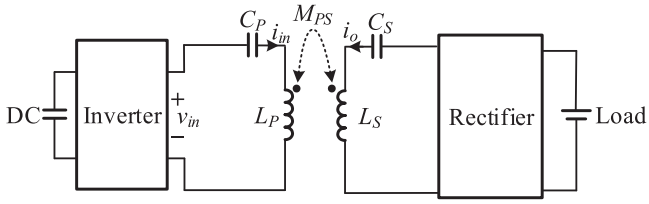

Fig. 2. Circuit topology of an SS WPT system.

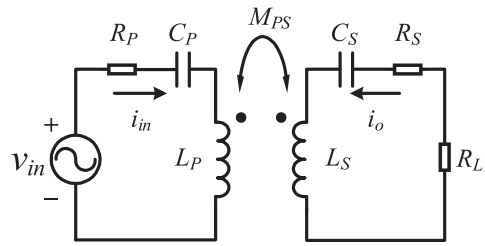

Fig. 3. FHA circuit model of an SS WPT system.

TABLE I
Parameters of the Example SS WPT System

Litz wire structure	0.1 mm × 500 (Φ 3.3 mm)	No. of turns	30
Coil outer dimension	350 mm × 350 mm	Coil inner dimension	152 mm × 152 mm
Ferrite dimension	350 mm × 350 mm×5 mm	Aluminum Shield dimension	350 mm × 350 mm×3 mm
Coil and ferrite clearance	2 mm	Ferrite and aluminum clearance	20 mm
L_P and L_S	485 μH	C_P and C_S	7.2 nF
R_L	39.3 Ω		

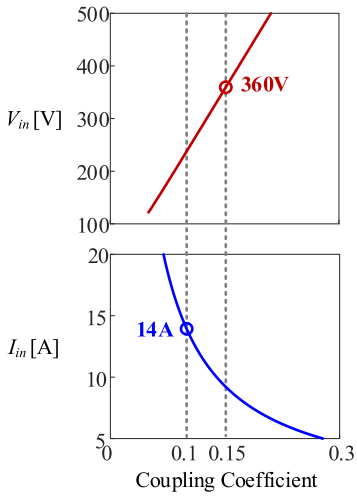

Fig. 4. Required input voltage and current to output the rated power as the coupling coefficient changes in the example SS WPT system.

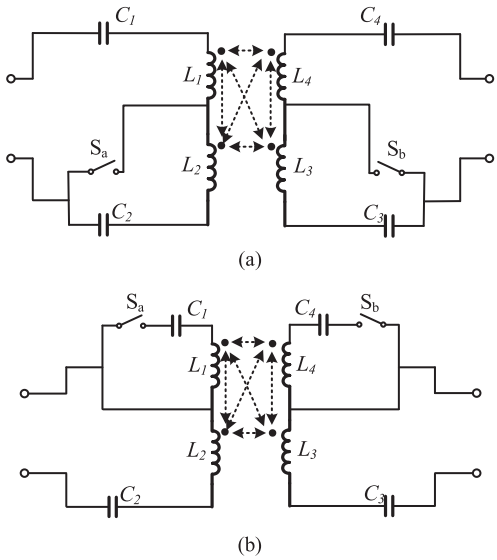

Fig. 5. Conceptual reconfigurable resonant topology. (a) Two switches located at the common paths of two resonators. (b) Two switches located at the noncommon paths of the resonators.

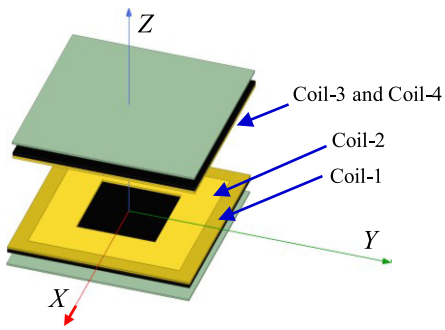

Fig. 6. Coupler structure for the proposed reconfigurable resonant topology.

Operating at the resonant frequency, the coupling range in which an SS WPT system can output a required power is determined by the input voltage and current limits of the system. For a dc input voltage of 400 V, the rms value of the fundamental component of the inverter output voltage is approximately 360 V, which is the input voltage upper limit. To provide a VA rating of 1.5 times the rated power (3.3 kW), the input rms current limit is set at 14 A. Fig. 4 shows the required input voltage and current of the example SS system to output 3.3 kW at an output voltage of 400 V. As the coupling becomes stronger, the SS system (operating at the resonant frequency) transfers less power. Therefore, the input voltage must be increased to maintain the required output power. In this example system, the upper limit of the coupling coefficient is 0.15. With a coupling coefficient larger than 0.15, the input voltage will not be sufficient for generating 3.3 kW output power. On the other hand, if the coupling becomes weaker, the primary coil current will be larger for the same output power. Within the said current limit of 14 A, the lower limit of the coupling coefficient is 0.1. This coupling coefficient range of 0.1–0.15 is corresponding to an air gap range of 175–215 mm (i.e., 40 mm full-power air gap) in this system without misalignments.

III. Reconfigurable Resonant Topology

Fig. 5 shows the proposed reconfigurable resonant topology, and Fig. 6 shows the corresponding coupler structure. In Fig. 6, the original primary coil of a conventional two-coil WPT system splits into two coils, coil-1 and coil-2; similarly, the original secondary coil splits into two coils, coil-3 and coil-4. Coil-1, -2, -3, and -4 correspond to L_1, L_2, L_3, L_4, as shown in Fig. 5. Two switches, one in the primary side and one in the secondary side, are used to determine whether the two same-side coils are working in series or not. In Fig. 5(a), the switches are located at the common path of the two same-side resonators. For example, S_a is in the loop of resonator L_1–C_1 and also the loop of resonator L_2–C_2. When S_a is switched OFF, L_1 is in series of L_2, which is actually the original primary coil before splitting; When S_a is switched ON, resonator L_1–C_1 is connected to the power supply, while resonator L_2–C_2 plays as a relay resonator. Another possible structure is shown in Fig. 5(b), where the switches are located only in one of the same-side resonator loops. When the switch is ON, the circuit is the same, as shown in Fig. 5(a), but when the switch is OFF, only one of the split coils is activated, which is different from that in Fig. 5(a). Table II lists the operation modes of the proposed topology in Fig. 5(a), where 0 means the switch is OFF and 1 means ON.

In practical implementation, one challenge is to realize zero-voltage switching (ZVS) ON for the primary inverter, which is essential for high efficiency and stable operation, in all four operation modes. More compensating components are required to address this issue. For example, a topology for implementation is proposed in Fig. 7, with two more inductors and two single-pole double throw (SPDT) switches. The rest of this article will focus on this practical topology. The analysis of each operation mode is provided as follows.

TABLE II
OPERATION MODES OF THE PROPOSED RECONFIGURABLE RESONANT TOPOLOGY IN FIG. 5(A)

Mode	S_a	S_b	Operation Mode
1-to-1 Mode	0	0	Resoantor-1 and -2 are in series, and Resonator-3 and -4 are in series, forming a conventional 2-resonator system.
2-to-1 Mode	1	0	Resonator-1 is connected to the power source and Resonator-2 forms a relay resonator; Resonator-3 and -4 is in series and connected to the load.
1-to-2 Mode	0	1	Resonator-1 and -2 are in series and connected to the power source; Resonator-3 forms a relay resonator and Resonator-4 is connected to the load.
2-to-2 Mode	1	1	Resonator-1 is connected to the power source and Resonator-2 forms a relay resonator; Resonator-3 forms another relay resonator and Resonator-4 is connected to the load.

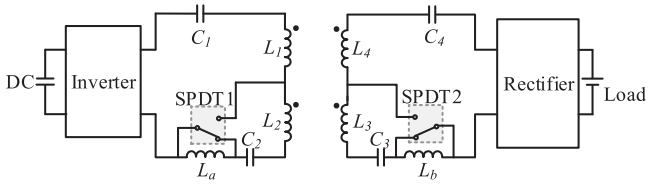

Fig. 7. One practical implementation of the proposed reconfigurable topology.

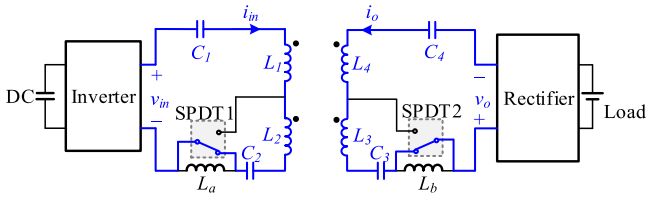

Fig. 8. Connection of the 1-to-1 mode.

A. Operation Modes Analysis

1) 1-to-1 Mode: The connection of the 1-to-1 mode is given in Fig. 8, which is basically a conventional two-coil WPT system. In Fig. 8, $v_{\rm in}$ and $i_{\rm in}$ are the input voltage and input current applied to the primary resonator, respectively, and the rms values of their fundamental components are denoted as $V_{\rm in}$ and $I_{\rm in}$, respectively; v_o and $i_{\rm in}$ are the output voltage and output current fed into the rectifier, respectively, and the rms values of their fundamental components are denoted as V_o and I_o, respectively. Use R_L to denote the equivalent ac load resistance, which is given by [33]

$$R_L = \frac{V_O}{I_O}. \tag{3}$$

Use the subscripts P and S to denote the variables of the primary and secondary sides, respectively. Therefore

$$L_P = L_1 + L_2 + 2M_{12} \tag{4}$$

$$L_S = L_3 + L_4 + 2M_{34} \tag{5}$$

$$M_{PS} = M_{13} + M_{14} + M_{23} + M_{24} \tag{6}$$

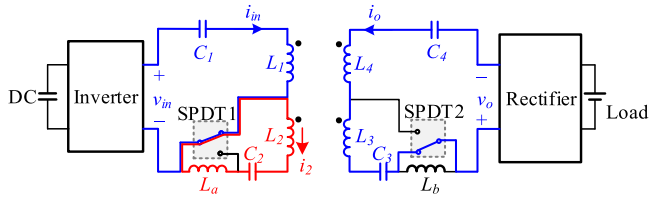

Fig. 9. Connection of the 2-to-1 mode.

where M_{ij} ($i, j = 1, 2, 3,$ or 4) is the mutual inductance between coil-i and coil-j; M_{PS} is the mutual inductance between two original coils before splitting.

For high efficiency and zero-phase-angle (ZPA, [5]) operation, the primary and secondary resonators should resonate at the operating frequency [5], i.e.,

$$X_P = \omega L_P - \frac{1}{\omega C_1} - \frac{1}{\omega C_2} = 0 \tag{7}$$

$$X_S = \omega L_S - \frac{1}{\omega C_3} - \frac{1}{\omega C_4} = 0. \tag{8}$$

By neglecting the power losses of the resonators, the input impedance of the system is given by

$$Z_{\rm in} = \frac{\omega^2 M_{PS}^2}{R_L} \tag{9}$$

and the input voltage can be derived from (1) as

$$V_{\rm in} = \omega M_{PS} I_O \tag{10}$$

and the input current can be derived from (2) as

$$I_{\rm in} = \frac{V_O}{\omega M_{PS}}. \tag{11}$$

The limits of the input voltage and input currents are given by

$$V_{\rm in} < V_{\rm in\,max} \tag{12}$$

$$I_{\rm in} < I_{\rm in\,max}. \tag{13}$$

With ZPA operation and for the given minimum power, (13) is equivalent to

$$V_{\rm in} > V_{\rm in\,min} = \frac{P_O}{I_{\rm in\,max}} \tag{14}$$

where $V_{\rm in\ min}$ is the minimal input voltage.

The impedance is limited as follows:

$$\frac{V_{\rm in\,min}^2}{P_O} < Z_{\rm in} < \frac{V_{\rm in\,max}^2}{P_O}. \tag{15}$$

Combining (10)–(12) and (14), the mutual inductance range for full-power operation under the input voltage and current limits is

$$\frac{V_{\rm in\,min}}{\omega I_O} \le M_{PS} \le \frac{V_{\rm in\,max}}{\omega I_O}. \tag{16}$$

2) 2-to-1 Mode: In this mode, L_a participates in the resonance of resonator-2; L_b is bypassed, as shown in Fig. 9. Neglecting the parasitic resistances, the circuit equations of this mode are as follows:

$$jX_1\mathbf{I_{in}} + j\omega M_{12}\mathbf{I}_2 + j\omega M_{1S}\mathbf{I}_O = \mathbf{V_{in}} \tag{17}$$

$$j\omega M_{12}\mathbf{I_{in}} + jX_2\mathbf{I}_2 + j\omega M_{2S}\mathbf{I}_O = \mathbf{0} \tag{18}$$

$$j\omega M_{1S}\mathbf{I_{in}} + j\omega M_{2S}\mathbf{I}_2 + (R_L + jX_S)\mathbf{I}_O = \mathbf{0} \tag{19}$$

where

$$M_{1S} = M_{13} + M_{14} \tag{20}$$

$$M_{2S} = M_{23} + M_{24} \tag{21}$$

$$X_1 = \omega L_1 - \frac{1}{\omega C_1} \tag{22}$$

$$X_2 = \omega(L_2 + L_a) - \frac{1}{\omega C_2} = 0. \tag{23}$$

The input impedance of this mode can be derived as

$$Z_{\text{in}} = jX_1 + \frac{M_{12}^2 R_L - j2\omega M_{12}M_{1S}M_{2S}}{M_{2S}^2}. \tag{24}$$

By solving $\text{Im}(Z_{\text{in}}) = 0$, the required X_1 to realize ZPA is derived as

$$X_1 = \frac{2\omega M_{12}M_{1S}}{M_{2S}}. \tag{25}$$

With (25), the input impedance becomes

$$Z_{\text{in}} = \frac{M_{12}^2}{M_{2S}^2}R_L. \tag{26}$$

With (12), (14), and (26), the constraint of the mutual inductances of this mode can be derived as

$$\frac{V_O}{V_{\text{in max}}} \le \frac{M_{2S}}{M_{12}} \le \frac{V_O}{V_{\text{in min}}}. \tag{27}$$

3) 1-to-2 Mode: In this mode, L_a is bypassed and L_b participates in the resonance of resonator-3. Neglecting the parasitic resistances, the circuit equations of this mode are as follows:

$$jX_P\mathbf{I}_1 + j\omega M_{P3}\mathbf{I}_3 + j\omega M_{P4}\mathbf{I}_O = \mathbf{V_{in}} \tag{28}$$

$$j\omega M_{P3}\mathbf{I_{in}} + jX_3\mathbf{I}_3 + j\omega M_{34}\mathbf{I}_O = \mathbf{0} \tag{29}$$

$$j\omega M_{P4}\mathbf{I_{in}} + j\omega M_{34}\mathbf{I}_3 + (R_L + jX_4)\mathbf{I}_O = \mathbf{0} \tag{30}$$

where

$$M_{P3} = M_{13} + M_{23} \tag{31}$$

$$M_{P4} = M_{14} + M_{24} \tag{32}$$

$$X_3 = \omega(L_3 + L_b) - \frac{1}{\omega C_3} \tag{33}$$

$$X_4 = \omega L_4 - \frac{1}{\omega C_4} = 0. \tag{34}$$

To ensure a high transfer efficiency, the receiving resonator connected to the load is still working at its resonant frequency, i.e., $X_4 = 0$. The input impedance of the system is derived as

$$Z_{\text{in}} = \frac{\omega^2 M_{P3}^2 R_L + j(\omega^2 M_{P4}^2 X_3 - 2\omega^3 M_{P3}M_{P4}M_{34})}{\omega^2 M_{34}^2 + jX_3 R_L}. \tag{35}$$

To realize ZPA, the compensating state of the relay resonator, i.e., resonator-3, as shown in Fig. 10, should be adjusted. By

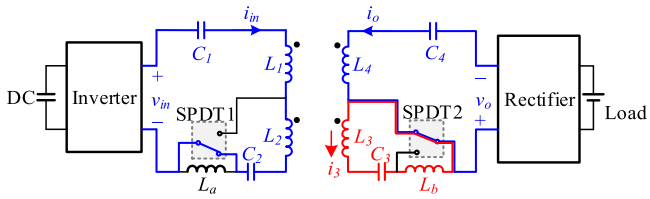

Fig. 10. Connection of the 1-to-2 mode.

solving $\text{Im}(Z_{\text{in}}) = 0$, the X_3 that can realize ZPA can be derived as

$$X_3 = \frac{2\omega^3 M_{P3}M_{P4}M_{34}^3}{\omega^2 M_{P4}^2 M_{34}^2 - M_{P3}^2 R_L^2}. \tag{36}$$

Then, the input impedance becomes

$$Z_{\text{in}} = \frac{\omega^4 M_{P3}^2 M_{34}^2 R_L + X_3 R_L(\omega^2 M_{P4}^2 X_3 - 2\omega^3 M_{P3}M_{P4}M_{34})}{\omega^4 M_{34}^4 + X_3^2 R_L^2}. \tag{37}$$

With (12), (14), and (37), the mutual inductance range for full-power operation under the input voltage and current limits is determined by

$$\frac{V_{\text{in min}}^2}{V_O^2} \le \left|\frac{Z_{\text{in}}}{R_L}\right| \le \frac{V_{\text{in max}}^2}{V_O^2}. \tag{38}$$

4) 2-to-2 Mode: The 2-to-2 mode is a four-resonator system, which can be described with the following circuit equations:

$$jX_1\mathbf{I_{in}} + j\omega M_{12}\mathbf{I}_2 + j\omega M_{13}\mathbf{I}_3 + j\omega M_{14}\mathbf{I}_O = \mathbf{V_{in}} \tag{39}$$

$$j\omega M_{12}\mathbf{I_{in}} + jX_2\mathbf{I}_2 + j\omega M_{23}\mathbf{I}_3 + j\omega M_{24}\mathbf{I}_O = \mathbf{0} \tag{40}$$

$$j\omega M_{13}\mathbf{I_{in}} + j\omega M_{23}\mathbf{I}_2 + jX_3\mathbf{I}_3 + j\omega M_{34}\mathbf{I}_O = \mathbf{0} \tag{41}$$

$$j\omega M_{14}\mathbf{I_{in}} + j\omega M_{24}\mathbf{I}_2 + j\omega M_{34}\mathbf{I}_3 + (R_L + jX_4)\mathbf{I}_O = \mathbf{0} \tag{42}$$

where X_1 is determined by (25); $X_2 = 0$; X_3 is determined by (36); $X_4 = 0$. The output power is given by

$$P_O = \frac{V_{\text{in}}^2(M_{23}^2 R_L^2 + 4\omega^2 M_{24}^2 M_{34}^2)}{R_L\omega^2(M_{12}M_{34} + M_{13}M_{24} - M_{14}M_{23})^2} = \frac{I_{\text{in}}^2 R_L \omega^2 (M_{12}M_{34} + M_{13}M_{24} - M_{14}M_{23})^2}{M_{23}^2 R_L^2 + 4\omega^2 M_{24}^2 M_{34}^2}. \tag{43}$$

Thus, the mutual inductance range for full-power operation under the input voltage and current limits is determined by

$$\frac{V_O^2}{V_{\text{in max}}^2} \le \frac{(M_{23}^2 R_L^2 + 4\omega^2 M_{24}^2 M_{34}^2)}{\omega^2(M_{12}M_{34} + M_{13}M_{24} - M_{14}M_{23})^2} \le \frac{V_O^2}{V_{\text{in min}}^2}. \tag{44}$$

5) Summary of Calculating the Values of the Compensating Components: The known parameters in the compensation network are the self-inductances and mutual inductances of the

coils, which can be obtained with finite-element analysis tool. The unknown variables in the compensation network are C_{1-4}, L_a, and L_b. The procedure of calculating these six unknown variables is described as follows.

a) In the 1-to-2 mode and the 2-to-2 mode, L_4 and C_4 are resonant at the operating frequency, and thereby, C_4 is determined with (34).
b) In the 1-to-1 mode and the 2-to-1 mode, C_3 in series with C_4 are resonant with L_S, and thereby, C_3 is determined with (8).
c) In the 1-to-2 mode, L_b is set at a value for ensuring ZPA and so L_b is determined with (33) and (36).
d) In the 2-to-1 mode, C_1 is adjusted to realize ZPA, and thereby, C_1 is calculated with (22) and (25).
e) In the 1-to-1 mode and the 1-to-2 mode, C_1 in series with C_2 are resonant with L_P, and thereby, C_2 is determined with (7).
f) In the 2-to-1 mode and the 2-to-2 mode, L_a, L_2, and C_2 are resonant, and thereby, L_a is calculated with (23).

B. Voltage and Current Stresses of SPDT1 and SPDT2

1) 1-to-1 Mode: Referring to Fig. 8, the current flowing through one switch of SPDT1 is $\mathbf{I_{in}}$, and the voltage across the other switch of SPDT1 is given by

$$\mathbf{V_{1-to-1,SPDT1}} = j(\omega L_2 - \frac{1}{\omega C_2})\mathbf{I_{in}} + j\omega M_{12}\mathbf{I_{in}} + j\omega\left(M_{23}+M_{24}\right)\mathbf{I_O}. \quad (45)$$

Combining (2) and (8), it can be rewritten as

$$\mathbf{V_{1-to-1,SPDT1}} = \left[j(\omega L_2 - \frac{1}{\omega C_2}) + j\omega M_{12} + \frac{\omega^2 M_{PS}\left(M_{23}+M_{24}\right)}{R_L}\right]\mathbf{I_{in}}. \quad (46)$$

Similarly, the current flowing through one switch of SPDT2 is $\mathbf{I_O}$, and the voltage across the other switch of SPDT2 is derived as

$$\mathbf{V_{1-to-1,SPDT2}} = \left\{\begin{array}{c}\left[(\omega L_3 - \frac{1}{\omega C_3}) + \omega M_{34}\right]\frac{\omega M_{PS}}{R_L} \\ +j\omega\left(M_{13}+M_{23}\right)\end{array}\right\}\mathbf{I_{in}}. \quad (47)$$

2) 2-to-1 Mode: Referring to Fig. 9, the current flowing through one switch of SPDT1 is the combination of $\mathbf{I_{in}}$ and $\mathbf{I_2}$, i.e.,

$$\mathbf{I_{2-to-1,SPDT1}} = \mathbf{I_{in}} - \mathbf{I_2}. \quad (48)$$

Combining (18) and (19), $\mathbf{I_2}$ can be solved as

$$\mathbf{I_2} = -\frac{\omega M_{1S}M_{2S} + jM_{12}R_L}{\omega M_{2S}^2}\mathbf{I_{in}}. \quad (49)$$

Then, (48) can be rewritten as

$$\mathbf{I_{2-to-1,SPDT1}} = \frac{\omega M_{2S}\left(M_{1S}+M_{2S}\right) + jM_{12}R_L}{\omega M_{2S}^2}\mathbf{I_{in}}. \quad (50)$$

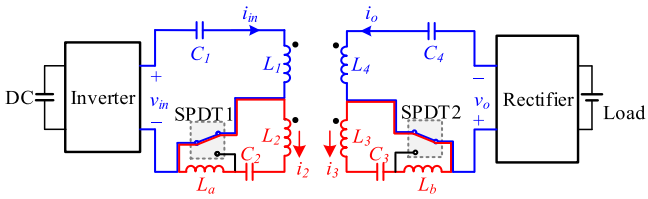

Fig. 11. Connection of the 2-to-2 mode.

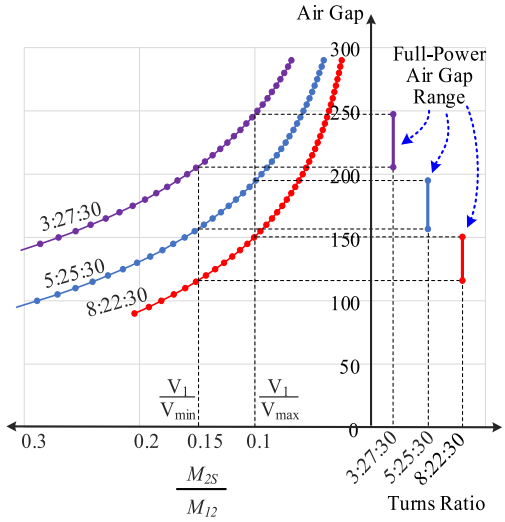

Fig. 12. Determine the full-power air gap ranges of the 2-to-1 mode with different turns ratios.

The voltage across the other switch of SPDT1 equals the voltage across L_a, i.e.,

$$\mathbf{V_{2-to-1,SPDT1}} = \omega L_a \mathbf{I_2} \quad (51)$$

which can be rewritten as

$$\mathbf{V_{2-to-1,SPDT1}} = -L_a\frac{\omega M_{1S}M_{2S} + jM_{12}R_L}{M_{2S}^2}\mathbf{I_{in}}. \quad (52)$$

The current flowing through one switch of SPDT2 is $\mathbf{I_O}$, and the voltage is derived as

$$\mathbf{V_{2-to-1,SPDT2}} = \left\{\begin{array}{c}\frac{M_{12}M_{23}R_L}{M_{2S}^2} + j\omega M_{13} - j\frac{\omega M_{1S}M_{23}}{M_{2S}} \\ -j\frac{M_{12}}{M_{2S}}\left[(\omega L_3 - \frac{1}{\omega C_3}) + \omega M_{34}\right]\end{array}\right\}\mathbf{I_{in}}. \quad (53)$$

3) 1-to-2 Mode: Referring to Fig. 10, the current flowing through one switch of SPDT1 is $\mathbf{I_{in}}$, and the voltage across the other switch of SPDT1 is given by (45). With (28)–(30), $\mathbf{I_{in}}$ and $\mathbf{I_O}$can be solved, and the voltage of SPDT1 can be calculated with (45).

For SPDT2, the current is the combination of $\mathbf{I_{in}}$ and $\mathbf{I_2}$, i.e.,

$$\mathbf{I_{1-to-2,SPDT2}} = \mathbf{I_O} - \mathbf{I_3}. \quad (54)$$

Combining (29) and (30), $\mathbf{I_3}$ can be solved as

$$\mathbf{I_3} = \frac{\omega M_{34}M_{P4} + jM_{P3}R_L}{\omega M_{34}M_{P3} - M_{P4}X_3}\mathbf{I_O}. \quad (55)$$

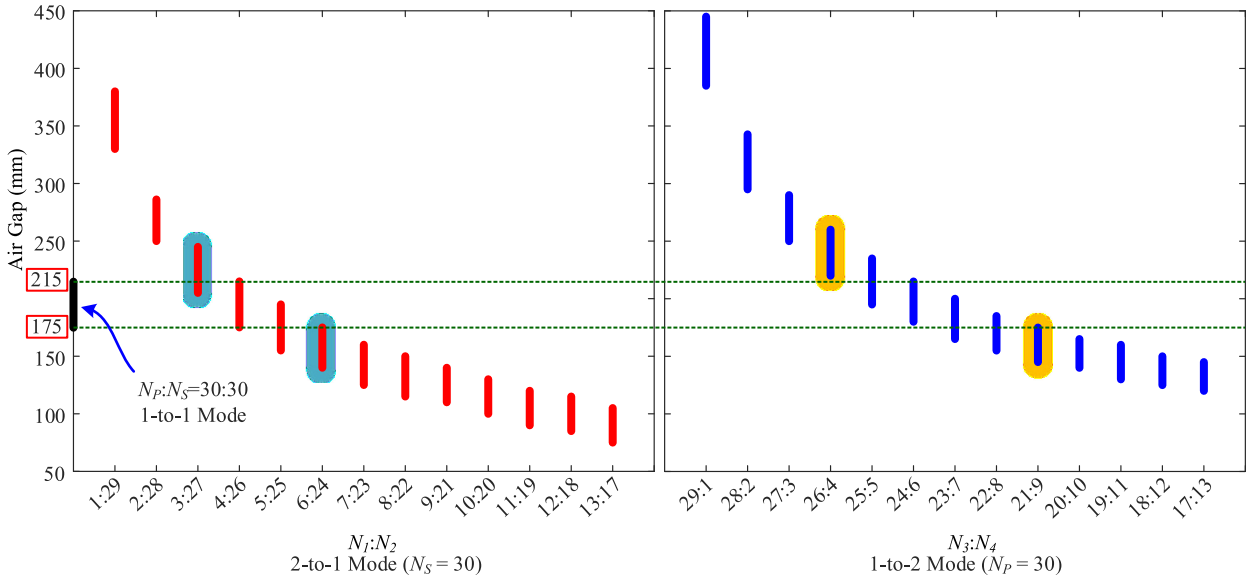

Fig. 13. Full-power air gap ranges of the 1-to-1, 2-to-1, and 1-to-2 modes with different turns ratios.

Then, (54) can be rewritten as

$$\mathbf{I_{1-to-2,SPDT2}} = \frac{\omega M_{34}(M_{P3}-M_{P4}) - M_{P4}X_3 - jR_L M_{P3}}{\omega M_{34}M_{P3} - M_{P4}X_3}\mathbf{I_O}. \quad (56)$$

The voltage across the other switch of SPDT2 equals the voltage across L_b, i.e.,

$$\mathbf{V_{1-to-2,SPDT2}} = \omega L_b \mathbf{I_3} \quad (57)$$

which can be rewritten as

$$\mathbf{V_{1-to-2,SPDT2}} = \omega L_b \frac{\omega M_{34}M_{P4} + jM_{P3}R_L}{\omega M_{34}M_{P3} - M_{P4}X_3}\mathbf{I_O}. \quad (58)$$

4) 2-to-2 Mode: Referring to Fig. 11, the current flowing through SPDT1 is given by (48), and the voltage is given by (51). For SPDT2, the current is given by (54), and the voltage is given by (57). After the currents are calculated with the equations of (39)–(42), the voltage and current stresses of SPDT1 and SPDT2 can be calculated.

C. Full-Power Coupling Range

Based on the same 30-turn coil described in Table I, the splitting ratios of the primary and secondary coils and the respective full-power coupling range of the four operation modes are investigated. To simplify the analysis, misalignment is not considered in this study and, thus, only air gap changes.

The full-power coupling range of the 1-to-1 mode is given by (16) and it is 175–215 mm in terms of the air gap range as discussed in Section II. The full-power air gap range of the 2-to-1 mode can be obtained, as shown in Fig. 12. In this mode, the ratio between the mutual inductance of coil-2 and coil-*S* (i.e., M_{2S}) and that of coil-1 and coil-2 (i.e., M_{12}) is in the range given by (27), which can be calculated as 0.1–0.15, for full-power operation under the input voltage and current limits. This range is corresponding to a different air gap range for each given turns ratio, as shown in Fig. 12. For example, for turns ratio of N_1:N_2:N_S = 3:27:30, the full-power air gap range is about 206–247 mm. Similarly, the full-power air gap ranges of the 1-to-2 mode can be identified with the help of (38).

D. Linking Operation Modes

With the above method to determine the full-power coupling ranges of the 1-to-1, 2-to-1, and 1-to-2 modes, we now consider how to link the four modes so that they can perfectly cover a large coupling range. Also, take the system with the 30-turn coils as an example. According to (16), (27), and (38), the full-power air gap ranges of the 2-to-1 and 1-to-2 modes with different coil splitting ratios are obtained and visualized in Fig. 13. The full-power air gap range of the 1-to-1 mode is also shown in Fig. 13. The corresponding inductances with different coil splitting ratios are given in Fig. 14. It can be seen that to link the 1-to-1 mode with the 2-to-1 mode, the splitting ratio of the primary coil should be N_1:N_2 = 3:27 or 6:24; to link the 1-to-1 mode with the 1-to-2 mode, the splitting ratio of the secondary coil should be N_3:N_4 = 26:4 or 21:9.

To perfectly link all the four operation modes, the 1-to-1 mode should be at least linked to either the 2-to-1 mode or the 1-to-2 mode. Therefore, the splitting ratio of the primary coil is first set at 3:27 or 6:24 to link the 1-to1 mode and the 2-to-1 mode, and the full-power air gap ranges of the other two modes are plotted, as shown in Fig. 15, as the splitting ratio of the secondary coil (i.e., N_3:N_4) changes. Then, the splitting ratio of the secondary coil is set at 26:4 or 21:9 to link the 1-to-1 mode and the 1-to-2 mode. Combining (44), the full-power air gap ranges of the other two modes are plotted in Fig. 16. From Figs. 15 and 16, the possible turns ratios that can connect all the four operation modes with minimal overlaps and gaps are as follows.

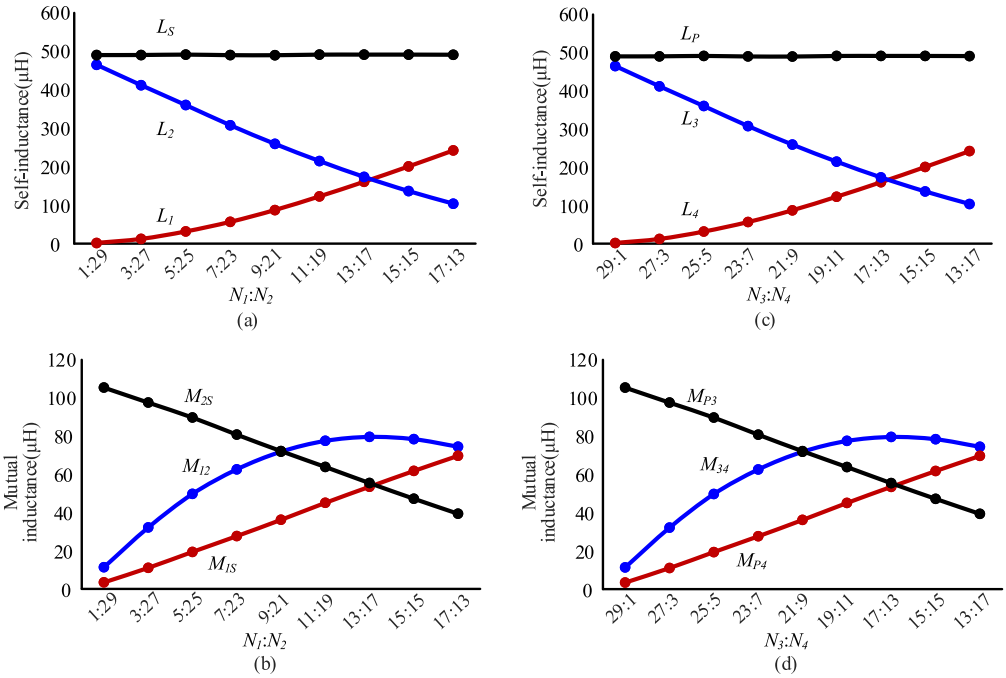

Fig. 14. Inductance changes with turns ratio in the 2-to-1 and 1-to-2 modes. (a) 2-to-1 mode ($N_S = 30$, air gap = 140 mm). (b) 2-to-1 mode ($N_S = 30$, air gap = 140 mm). (c) 1-to-2 mode ($N_P = 30$, air gap = 140 mm). (d) 1-to-2 mode ($N_P = 30$, air gap = 140 mm).

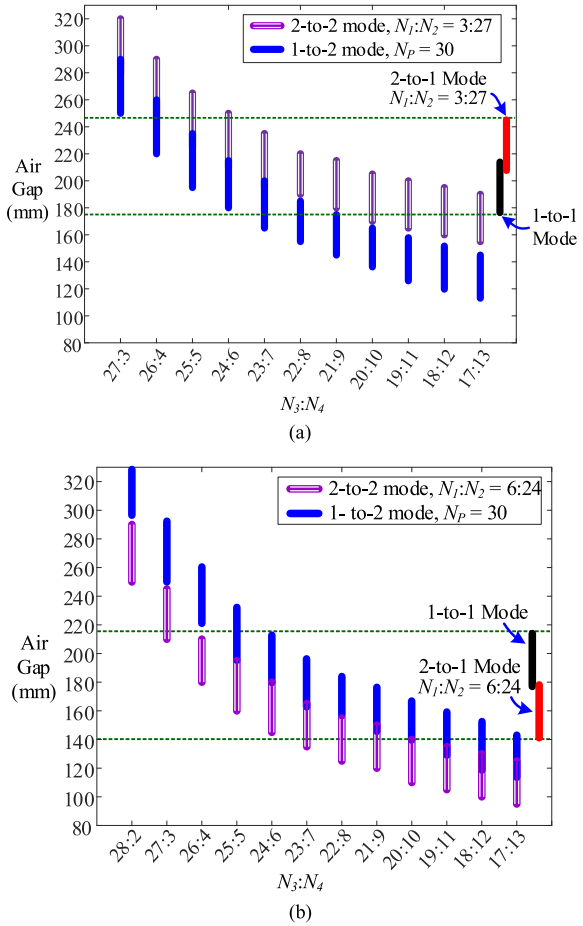

Fig. 15. Full-power air gap ranges of the 1-to-2 and 2-to-2 modes with fixed N_1:N_2 and varying N_3:N_4. (a) N_1:N_2 = 3:27. (b) N_1:N_2 = 6:24.

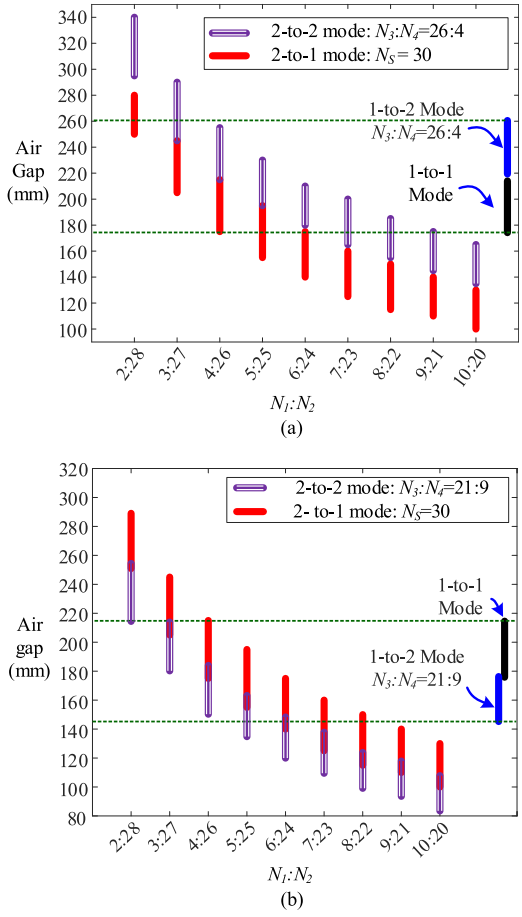

Fig. 16. Full-power air gap ranges of the 2-to-1 and 2-to-2 modes with fixed N_3:N_4 and varying N_1:N_2. (a) N_3:N_4 = 26:4. (b) N_3:N_4 = 21:9.

1) N_1:N_2:N_3:N_4 = 3:27:27:3 (air gap: 175–320 mm).
2) N_1:N_2:N_3:N_4 = 6:24:17:13 (air gap: 95–215 mm).
3) N_1:N_2:N_3:N_4 = 6:24:27:3 (air gap: 140–290 mm).
4) N_1:N_2:N_3:N_4 = 9:21:26:4 (air gap: 110–260 mm).
5) N_1:N_2:N_3:N_4 = 2:28:21:9 (air gap: 145–290 mm).
6) N_1:N_2:N_3:N_4 = 8:22:21:9 (air gap: 100–215 mm).

E. Process of Determining Turns Ratio

The process of determining the turns ratio, i.e., N_1:N_2:N_3:N_4, is summarized as follows.

1) The total numbers of turns of the primary windings and the secondary windings, i.e., N_P and N_S, are first supposed to be given by the application or designed as follows. Because the 1-to-1 mode ideally eliminates reactive power or circulating power, it is good assumption that this mode covers the weakest coupling region in the application. Based on this assumption and the basic theory of the conventional 1-to-1 SS WPT theory [4], N_P, N_S, and the full-power coupling range of this mode can be determined.
2) The full-power coupling ranges of the 2-to-1 mode and the 1-to-2 mode are found with different N_1:N_2 and N_3:N_4, following the procedure described in Section III-B.
3) The possible turns ratios of N_1:N_2 and N_3:N_4 are determined, which make the full-power coupling ranges of the 2-to-1 mode and the 1-to-2 mode favorably linking the full-power coupling range of the 1-to-1 mode.
4) The full-power coupling ranges of the 2-to-2 mode are obtained with the selected turns ratios of N_1:N_2 and N_3:N_4. Then, the possible turns ratios of N_1:N_2:N_3:N_4, which can link all four modes, are eventually found, as described in Section III-C. Among all possible solutions, the one that meets the coupling range requirement best is selected as the final design.

F. Discussion

It can be noticed from Figs. 13, 15, and 16 that there are similar patterns of the full-power air gap changing with the turns ratio. With increasing N_1:N_2, the full-power air gap decreases in both the 2-to-1 and 2-to-2 modes; with increasing N_3:N_4, the full-power air gap increases in both the 1-to-2 and 2-to-2 modes. For the 2-to-1 mode, this pattern can be analytically explained as follows.

With (26), the output power of the 2-to-1 mode is given by

$$P_O = \frac{M_{2S}^2}{M_{12}^2}\frac{V_{\text{in}}^2}{R_L}. \tag{59}$$

Therefore, the output power of this mode is determined by the ratio of M_{2S}/M_{12} and is not affected by M_{1S}. With a small N_1:N_2, such as 1:29, M_{12} is also small, as shown in Fig. 14. Therefore, the M_{2S} for outputting the rated power is also small, which means the rated power coupling is weak, and thus, the power transfer distance is large to output the same rated power when M_{12} is small. As N_1:N_2 increases to approaching 1:1, M_{12} also increases, and the corresponding M_{2S} for the rated output power increases as well, meaning the power transfer distance becomes smaller for the same rated output power. This is consistent with the results given in Fig. 13.

However, analytically explanations cannot be easily obtained for the 1-to-2 mode and the 2-to-2 mode. A qualitative hypothesis is provided instead. In the transmitter side of the 2-to-1 or 2-to-2 mode, coil-1 and coil-2 with a smaller N_1:N_2 perform as a boosting transformer to some extent. Thus, a higher voltage is applied to resonator-2 so that the same amount of power can be transmitted to a further position, no matter in what form the receiver is (i.e., either one resonator or multiple resonators). Similarly, the receiver side with larger N_3:N_4 acts as a step-down transformer, which also increases the full-power transfer distance.

TABLE III
INDUCTANCES FROM FINITE-ELEMENT METHOD (FEM) SIMULATIONS

Parameter	Air Gap 215 mm (μH)	Air Gap 145 mm (μH)
L_1	70.7	70.9
L_2	280	283
L_3	257	259
L_4	86.4	86.5
M_{12}	66.7	67.5
M_{13}	9.70	19.4
M_{14}	5.67	10.8
M_{23}	21.7	48.3
M_{24}	11.7	23.3
M_{34}	70.8	71.6

TABLE IV
COMPENSATING COMPONENTS

Parameter	Value	Parameter	Value
C_1	187.2 nF	C_4	40.5 nF
C_2	7.52 nF	L_a	183.6 μH
C_3	8.80 nF	L_b	70.7 μH

IV. SIMULATION AND EXPERIMENTAL VERIFICATIONS

A. Simulation Verification

Different turns ratios can be selected according to different applications to realize full-power transmission in a wide coupling range. To verify the design method and the operation of the reconfigurable topology, we take the turns ratio of 8:22:21:9 as an example. Finite-element simulation is done to obtain the inductances, as given in Table III. Following the procedure described in Section II-A, the values of the compensation components are determined as given in Table IV.

The simulation results obtained from circuit simulations are given in Fig. 17. Four operation modes cover an air gap range of 95–215 mm with slight power drops at 175 mm. Compared with the range of the conventional SS WPT system (i.e., 175–225 mm) under the same constraints, the full-power coupling range has been significantly improved.

B. Experimental Verification

A 3.3-kW prototype operating at a fixed frequency of 85 kHz has been built for experiments, as shown in Fig. 18(a). The primary winding structure is shown in Fig. 18(b) and the circuit connection follows Fig. 7. The turns ratio of the coils adopts

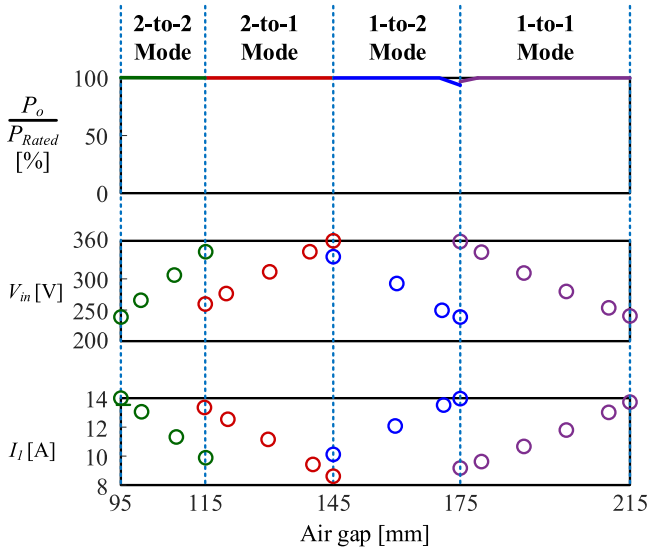

Fig. 17. Performance of the system with the proposed topology (simulation results).

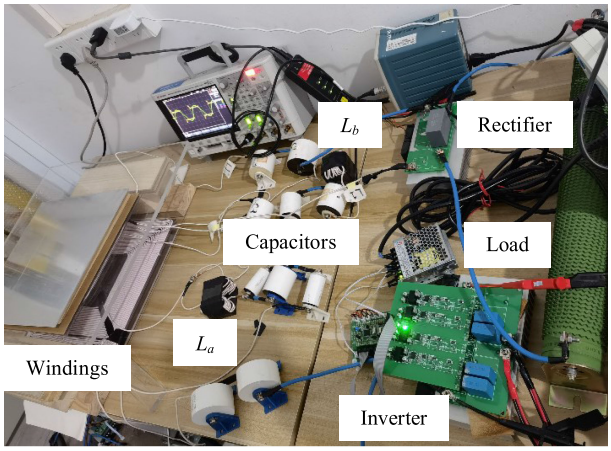

(a)

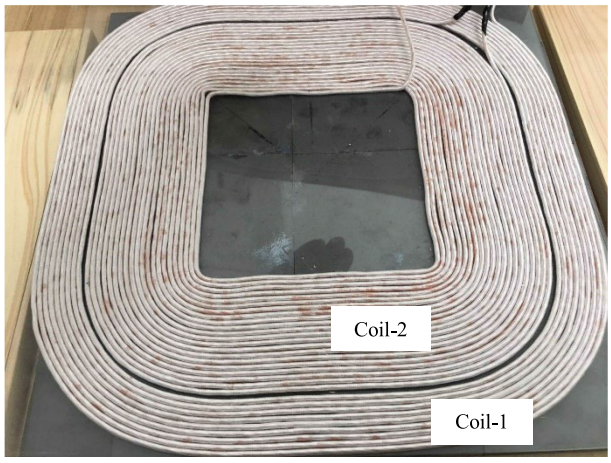

(b)

Fig. 18. Setup for experiments. (a) Experimental platform. (b) Primary coils of the prototype.

TABLE V
MEASURED INDUCTANCES (μH)

Air Gap	215 mm	140 mm	120 mm
L_1	69.0	69.0	69.8
L_2	270.5	270.4	272.6
L_3	251.0	254.1	257.6
L_4	85.0	85.6	86.44
M_{12}	64.1	64.7	66.3
M_{13}	5.86	21.0	25.9
M_{14}	9.51	12.2	15.1
M_{23}	20.9	52.6	68.3
M_{24}	11.8	26.4	33.3
M_{34}	70.0	72.1	72.8

TABLE VI
COMPENSATING CAPACITANCES AND INDUCTANCES

Parameter	Calculated Value	Parameter	Calculated Value
C_1	204nF	C_4	42.14nF
C_2	7.84nF	L_a	175μH
C_3	9.02nF	L_b	69μH

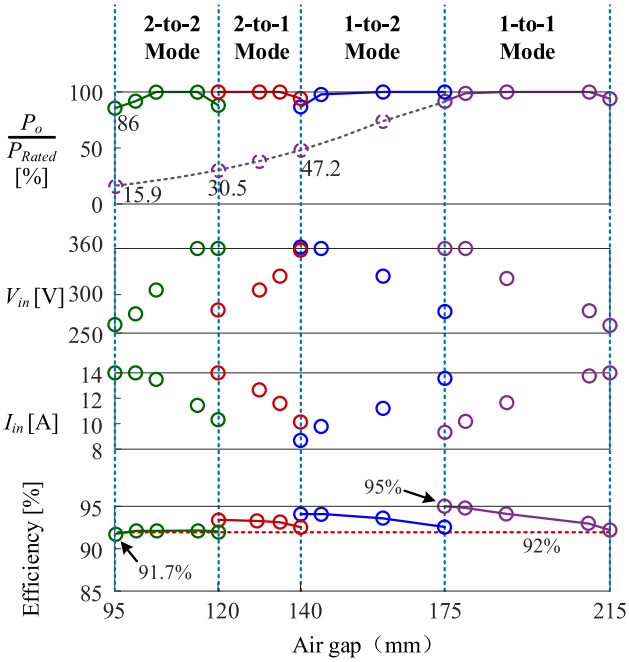

Fig. 19. Measured output power, input voltage, input current, and efficiency in the air gap range of 95–215 mm.

N_1:N_2:N_3:N_4 = 8:22:21:9. Coil-1 and coil-4 are the outer coils after splitting. The parameters of the compensation components are given in Tables V and VI. SiC MOSFET C2M0025120D and fast recovery diode IDW100E60 are used in the inverter and the rectifier, respectively.

The measured output power, which is normalized to the rated power, input voltage, input current, and dc–dc efficiency in the air gap range of 95–215 mm are given in Fig. 19, which are consistent with the simulation. The dashed line in the output power plot indicates the experimental output power of the traditional two-coil system. In general, the power transfer capability of the system with the proposed reconfigurable topology is

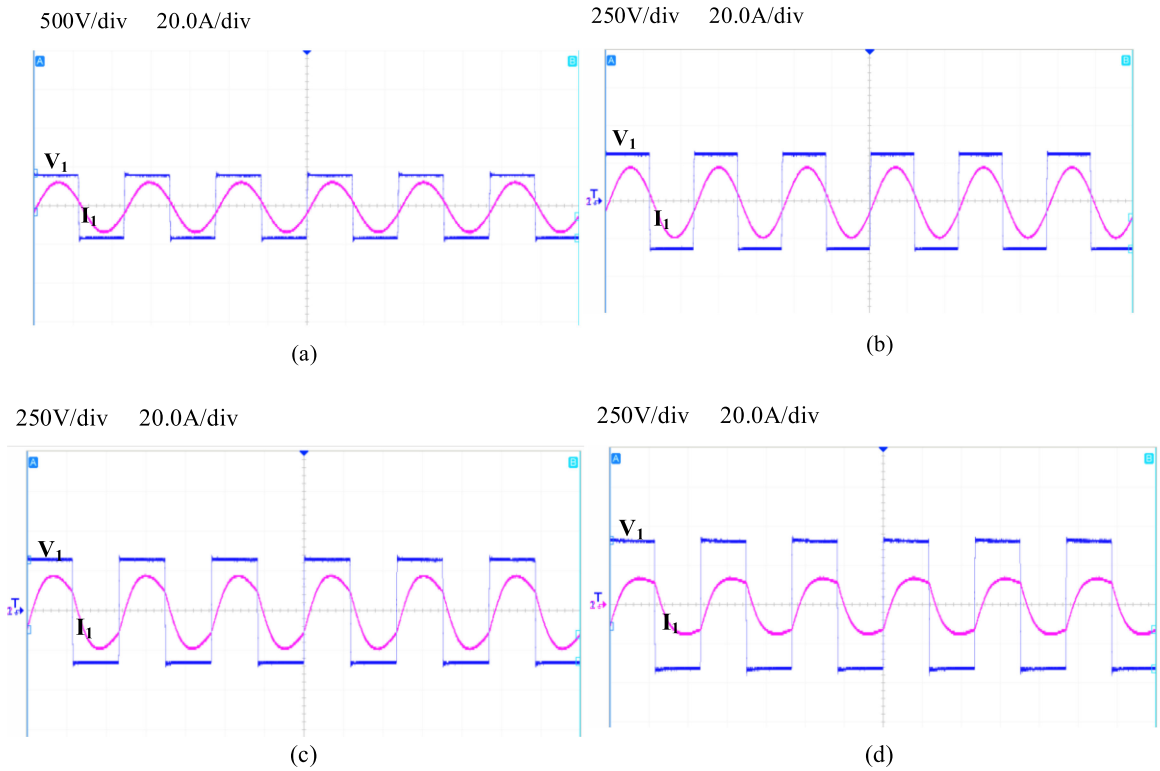

Fig. 20. Inverter output voltage and current waveforms. (a) 1-to-1 mode (air gap 175 mm). (b) 1-to-2 mode (air gap 175 mm). (c) 2-to-1 mode (air gap 120 mm). (d) 2-to-2 mode (air gap 120 mm).

TABLE VII
VOLTAGE AND CURRENT WAVEFORMS OF SPDT1 AND SPDT2

Mode (Air gap)	SPDT1		SPDT2	
	Simulation (500V/div; 10A/div)	Experiment (500V/div; 10A/div)	Simulation (500V/div; 10A/div)	Experiment (500V/div; 10A/div)
1-to-1 (215mm)	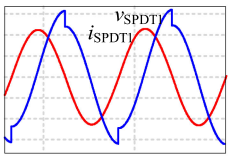	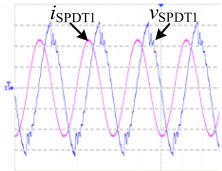	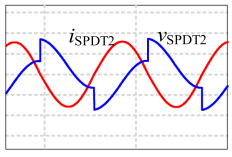	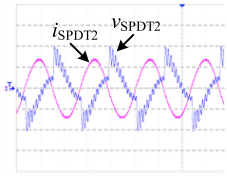
2-to-1 (140mm)	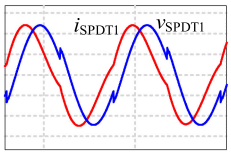	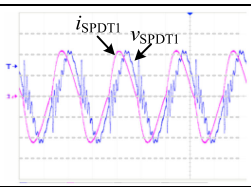	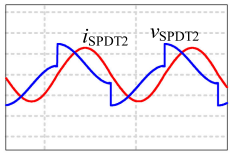	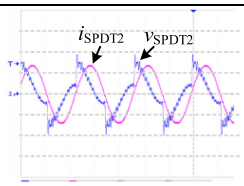
1-to-2 (140mm)	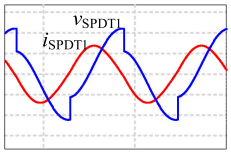	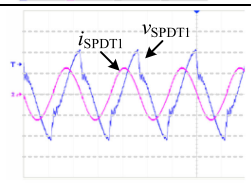	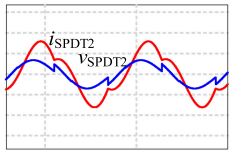	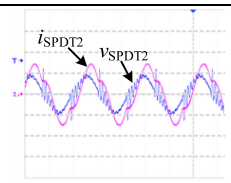
2-to-2 (120mm)	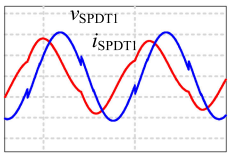	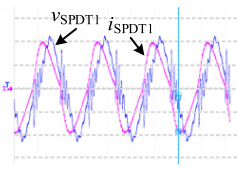	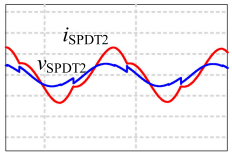	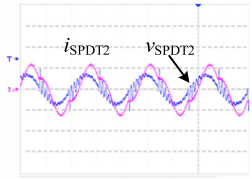

TABLE VIII
MEASURED VOLTAGE AND CURRENT STRESSES OF SPDT1, SPDT2, AND RESONANT COMPONENTS

RMS values	1-to-1 mode (air gap: 215mm)	1-to-2 mode (air gap: 140mm)	2-to-1 mode (air gap: 140mm)	2-to-2 mode (air gap: 120mm)
SPDT1	985V/14A	620V/9.0A	683V/15A	790V/13.2A
SPDT2	443V/8.6A	310V/9.4A	430V/9.7A	314V/9.5A
C_1	128.5V/14A	82.6V/9.0 A	91.8V/10A	92V/10A
C_2	3340V/14A	2150V /9.0A	2173V/9.1A	2126V/8.9A
C_3	1788V/8.6A	1515V /7.3A	1850V/8.9A	1600V/7.7A
C_4	382.87V/8.6A	378V /8.5A	395V/8.9A	382V/8.6A
L_a	0V/0A	0V/0A	683V /9.1A	695V/8.9A
L_b	0V/0A	310V/7.3A	0V/0A	314V/7.7A

significantly improved compared with the conventional two-coil system operating at a fixed frequency. The measured dc–dc efficiency in the given coupling range basically stay in the range of 92%–95%, as shown in Fig. 19. The inverter output voltage and current waveforms of the four operation modes are given in Fig. 20, showing that ZVS-ON is realized.

The measured voltage and current waveforms of SPDT1 and SPDT2 are given in Table VII, compared with the simulation results. The measured voltage and current stresses of the resonant components are given in Table VIII.

V. CONCLUSION

A reconfigurable resonant topology with two switches and four operation modes is proposed for WPT with a large air gap range. Considering to realize ZPA and ZVS-ON, one practical implementation of this concept is proposed, analyzed, and verified. With different connections of the switches, the proposed topology changes among four operation modes. Each operation mode is able to output the desired power in a specific air gap range under the input voltage and current limits, with a fixed switching frequency. By properly choosing the turns ratio of the coils, the full-power coupling ranges of four operation modes can be linked together and, thus, substantially enhance the power transfer capability of the system in a much wider air gap range. Both simulation and experiment show that this reconfigurable resonant topology is capable of high-efficiency WPT with a fixed switching frequency and with a large coupling range wider air gap range.

REFERENCES

[1] S. Y. R. Hui, "Magnetic resonance for wireless power transfer [A look back]," *IEEE Power Electron. Mag.*, vol. 3, no. 1, pp. 14–31, Mar. 2016.

[2] G. A. Covic and J. T. Boys, "Inductive power transfer," *Proc. IEEE*, vol. 101, no. 6, pp. 1276–1289, Jun. 2013.

[3] S. Li and C. C. Mi, "Wireless power transfer for electric vehicle applications," *IEEE J. Emerg. Sel. Topics Power Electron.*, vol. 3, no. 1, pp. 4–17, Mar. 2015.

[4] R. Bosshard and J. W. Kolar, "Multi-objective optimization of 50 kW/85 kHz IPT system for public transport," *IEEE J. Emerg. Sel. Topics Power Electron.*, vol. 4, no. 4, pp. 1370–1382, Dec. 2016.

[5] C.-S. Wang, G. A. Covic, and O. H. Stielau, "Power transfer capability and bifurcation phenomena of loosely coupled inductive power transfer systems," *IEEE Trans. Ind. Electron.*, vol. 51, no. 1, pp. 148–157, Feb. 2004.

[6] A. P. Sample, D. T. Meyer, and J. R. Smith, "Analysis, experimental results, and range adaptation of magnetically coupled resonators for wireless power transfer," *IEEE Trans. Ind. Electron.*, vol. 58, no. 2, pp. 544–554, Feb. 2011.

[7] W.-Q. Niu, J.-X. Chu, W. Gu, and A.-D. Shen, "Exact analysis of frequency splitting phenomena of contactless power transfer systems," *IEEE Trans. Circuits Syst. I, Reg. Papers*, vol. 60, no. 6, pp. 1670–1677, Jun. 2013.

[8] Y. Zhang and Z. Zhao, "Frequency splitting analysis of two-coil resonant wireless power transfer," *IEEE Antennas Wireless Propag. Lett.*, vol. 13, pp. 400–402, 2014.

[9] R. Huang and B. Zhang, "Frequency, impedance characteristics and HF converters of two-coil and four-coil wireless power transfer," *IEEE J. Emerg. Sel. Topics Power Electron.*, vol. 3, no. 1, pp. 177–183, Mar. 2015.

[10] J. Park, Y. Tak, Yoongoo Kim, Y. Kim, and S. Nam, "Investigation of adaptive matching methods for near-field wireless power transfer," *IEEE Trans. Antennas Propag.*, vol. 59, no. 5, pp. 1769–1773, May 2011.

[11] C.-S. Wang, G. A. Covic, and O. H. Stielau, "Investigating an *LCL* load resonant inverter for inductive power transfer applications," *IEEE Trans. Power Electron.*, vol. 19, no. 4, pp. 995–1002, Jul. 2004, doi: 10.1109/TPEL.2004.830098.

[12] N. A. Keeling, G. A. Covic, and J. T. Boys, "A unity-power-factor IPT pickup for high-power applications," *IEEE Trans. Ind. Electron.*, vol. 57, no. 2, pp. 744–751, Feb. 2010, doi: 10.1109/TIE.2009.2027255.

[13] J. L. Villa, J. Sallan, J. F. Sanz Osorio, and A. Llombart, "High-misalignment tolerant compensation topology for ICPT systems," *IEEE Trans. Ind. Electron.*, vol. 59, no. 2, pp. 945–951, Feb. 2012, doi: 10.1109/TIE.2011.2161055.

[14] Y. Wang, Y. Yao, X. Liu, and D. Xu, "S/*CLC* compensation topology analysis and circular coil design for wireless power transfer," *IEEE Trans. Transp. Electrific.*, vol. 3, no. 2, pp. 496–507, Jun. 2017, doi: 10.1109/TTE.2017.2651067.

[15] S. Li, W. Li, J. Deng, T. D. Nguyen, and C. C. Mi, "A double-sided *LCC* compensation network and its tuning method for wireless power transfer," *IEEE Trans. Veh. Technol.*, vol. 64, no. 6, pp. 2261–2273, Jun. 2015.

[16] W. Li, H. Zhao, S. Li, J. Deng, T. Kan, and C. C. Mi, "Integrated *LCC* compensation topology for wireless charger in electric and plug-in electric vehicles," *IEEE Trans. Ind. Electron.*, vol. 62, no. 7, pp. 4215–4225, Jul. 2015.

[17] Z. Pantic, S. Bai, and S. M. Lukic, "ZCS *LCC*-compensated resonant inverter for inductive-power-transfer application," *IEEE Trans. Ind. Electron.*, vol. 58, no. 8, pp. 3500–3510, Aug. 2011.

[18] Q. Zhu, L. Wang, Y. Guo, C. Liao, and F. Li, "Applying *LCC* compensation network to dynamic wireless EV charging system," *IEEE Trans. Ind. Electron.*, vol. 63, no. 10, pp. 6557–6567, Oct. 2016.

[19] B. Esteban, M. Sid-Ahmed, and N. C. Kar, "A comparative study of power supply architectures in wireless EV charging systems," *IEEE Trans. Power Electron.*, vol. 30, no. 11, pp. 6408–6422, Nov. 2015.

[20] T. C. Beh, M. Kato, T. Imura, S. Oh, and Y. Hori, "Automated impedance matching system for robust wireless power transfer via magnetic resonance coupling," *IEEE Trans. Ind. Electron.*, vol. 60, no. 9, pp. 3689–3698, Sep. 2013.

[21] J. Lee, Y.-S. Lim, W.-J. Yang, and S.-O. Lim, "Wireless power transfer system adaptive to change in coil separation," *IEEE Trans. Antennas Propag.*, vol. 62, no. 2, pp. 889–897, Feb. 2014.

[22] Y.-J. Kim, D. Ha, W. J. Chappell, and P. P. Irazoqui, "Selective wireless power transfer for smart power distribution in a miniature-sized multiple-receiver system," *IEEE Trans. Ind. Electron.*, vol. 63, no. 3, pp. 1853–1862, Mar. 2016.

[23] Y. Lim, H. Tang, S. Lim, and J. Park, "An adaptive impedance-matching network based on a novel capacitor matrix for wireless power transfer," *IEEE Trans. Power Electron.*, vol. 29, no. 8, pp. 4403–4413, Aug. 2014.

[24] J. Kim, W.-S. Choi, and J. Jeong, "Loop switching technique for wireless power transfer using magnetic resonance coupling," *Prog. Electromagn. Res.*, vol. 138, pp. 197–209, 2013.
[25] G. Lee, B. H. Waters, Y. G. Shin, J. R. Smith, and W. S. Park, "A reconfigurable resonant coil for range adaptation wireless power transfer," *IEEE Trans. Microw. Theory Techn.*, vol. 64, no. 2, pp. 624–632, Feb. 2016.
[26] J. Kim and J. Jeong, "Range-adaptive wireless power transfer using multiloop and tunable matching techniques," *IEEE Trans. Ind. Electron.*, vol. 62, no. 10, pp. 6233–6241, Oct. 2015.
[27] P. P. Mercier and A. P. Chandrakasan, "Rapid wireless capacitor charging using a multi-tapped inductively-coupled secondary coil," *IEEE Trans. Circuits Syst. I , Reg. Papers*, vol. 60, no. 9, pp. 2263–2272, Sep. 2013.
[28] Z. Dang, Y. Cao, and J. A. Abu Qahouq, "Reconfigurable magnetic resonance-coupled wireless power transfer system," *IEEE Trans. Power Electron.*, vol. 30, no. 11, pp. 6057–6069, Nov. 2015, doi: 10.1109/TPEL.2015.2422776.
[29] W. Zhong and S. Y. Hui, "Reconfigurable wireless power transfer systems with high energy efficiency over wide load range," *IEEE Trans. Power Electron.*, vol. 33, no. 7, pp. 6379–6390, Jul. 2018.
[30] A. Kurs, A. Karalis, R. Moffatt, J. D. Joannopoulos, P. Fisher, and M. Soljacıc, "Wireless power transfer via strongly coupled magnetic resonances," *Science*, vol. 317, no. 5834, pp. 83–86, Jul. 2007.
[31] W. X. Zhong, C. Zhang, X. Liu, and S. Y. R. Hui, "A methodology for making a three-coil wireless power transfer system more energy efficient than a two-coil counterpart for extended transfer distance," *IEEE Trans. Power Electron.*, vol. 30, no. 2, pp. 933–942, Feb. 2015.
[32] J. Hu, C. Lee, and H. H.-C. Lu, "Reconfigurable wireless power transfer systems for distance adaptation," in *Proc. IEEE Int. Symp. Circuits Syst.*, 2019, pp. 1–4, doi: 10.1109/ISCAS.2019.8702768.
[33] N. Mohan, T. M. Undeland, and W. P. Robbins, *Power Electronics: Converters, Applications, and Design*. New York, NY, USA: Wiley, 1995.
[34] *Wireless Power Transfer for Light-Duty Plug-In/Electric Vehicles and Alignment Methodology*. Warrendale, PA, USA: SAE, May 2016.
[35] W. Zhong, D. Xu, and R. S. Y. Hui, *Wireless Power Transfer: Between Distance and Efficiency*. Singapore: Springer, 2020.

Wenxing Zhong (Senior Member, IEEE) received the B.Eng. degree in electrical engineering from Tsinghua University, Beijing, China, in 2007, and the Ph.D. degree from the City University of Hong Kong, Hong Kong, in 2012.

He is currently a Professor with the Department of Electrical Engineering, Zhejiang University, Hangzhou, China. From March 2016 to May 2017, he was a Research Assistant Professor with the Department of Electrical and Electronic Engineering, University of Hong Kong, Hong Kong. His research interests include wireless power transfer and power electronics.

Dr. Zhong was the recipient of two Transactions First Prize Paper Awards from the IEEE Power Electronics Society.

Siyuan Zhang received the B.Eng. degree from the Shanghai University of Engineering Science, Shanghai, China, in 2018. He is currently working toward the M.Sc. degree with the Department of Electrical Engineering, Zhejiang University, Hangzhou, China.

His research interests include wireless power transfer technologies.

Min Chen (Senior Member, IEEEE) was born in China, in 1976. He received the B.S. and Ph.D. degrees in power electronics from the Department of Electrical Engineering, Zhejiang University, Hangzhou, China, in 1998 and 2004, respectively.

He is currently an Associate Professor with Zhejiang University. His research interests include power device packaging, high-frequency high-power conversion, and renewable energy power conversion system.

Dr. Chen is an Associate Editor for the IEEE OPEN JOURNAL OF POWER ELECTRONICS.

Mark Dehong Xu (Fellow, IEEE) received the Ph.D. degree from the Department of Electrical Engineering, Zhejiang University, Hangzhou, China, in 1989.

He has been a Full Professor with Zhejiang University since 1996. He was a Visiting Professor with the Department of Electrical Engineering, University of Tokyo, Japan, from May 1995 to June 1996, Center of Power Electronics System, Virginia Tech, USA, from June to December of 2000, and Power Electronics Lab, ETH, Zurich, from February to April of 2006. He has authored ten books and more than 200 IEEE journal or conference papers. He holds more than 40 patents. His interests include power electronics topology, control, and applications to renewable energy and energy efficiency.

Dr. Xu was the recipient of six IEEE Transaction or Conference Prize Paper Awards and IEEE PELS R.D. Middlebrook Achievement Award in 2016. He was an IEEE PELS Distinguish Lecturer from 2015 to 2018. He is an At-Large Adcom Member of the IEEE Power Electronics Society from 2020 to 2022. He is the Co-Editor-Chief for the IEEE OPEN JOURNAL OF POWER ELECTRONICS and an Associate Editor for the IEEE TRANSACTIONS ON POWER ELECTRONICS. He was the General Chair of the IEEE International Symposium on Industrial Electronics (ISIE2012, Hangzhou), IEEE International Symposium on Power Electronics for Distributed Generation Systems (PEDG2013, Arkansas), and IEEE International Power Electronics and Applications Conference (PEAC2018, Shenzhen).